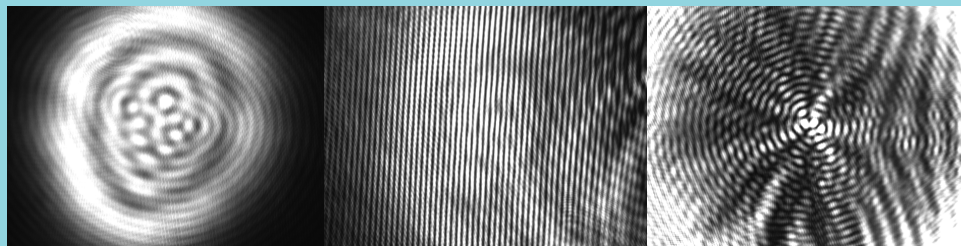# LUND UNIVERSITY
Faculty of Science

Construction and Characterization of an Interferometer for the Stabilization of Attosecond Experiments

Thomas K Jensen

Bachelor's Thesis

Supervisors: David Kroon and Anne L'Huillier

Abstract

A new optical interferometer for delay stabilization in attosecond pump/probe experiments is constructed, featuring a custom-made hole-drilled recombination mirror and using a co-propagating HeNe laser for the interference. The interferometer is shown to generate an interference pattern of high enough contrast for delay stabilization. The stability of the measured delay is tested with the interferometer in the passively stable mode. The measured delay is shown to exhibit four curious characteristics: a rapid fluctuation with $\sigma \approx 0.85\,\text{fs}$, sudden jumps of 2-4 fs, oscillations with a period of ~ 1 hour and amplitude of $\sim 4\,\text{fs}$, and a linear drift of varying magnitude. The rapid fluctuations are attributed to ambient vibrations and detector noise. The angular drift of the HeNe laser is shown to be an unlikely cause of the remaining effects. Further investigations of these are suggested. The interferometer design is recommended for further testing using active stabilization.

Populärvetenskaplig sammanfattning:
Det blåser i Atomen

Alla har vi väl någon gång cyklat till jobbet, eller till skolan för den delen. I glatt humör trampar man upp för stadens brantaste backe tills det plötsligt kommer en rejäl vindstöt - då står man på tramporna, flåsande. Man gör sitt bästa. Men man har vädrets makter emot sig. Så när man väl står där innanför personalkökets trygga väggar (eller föreläsningssalens) är kaffet sedan länge uppdrucket, frukten sönderskuren, upphackad och söndermald, och fjolårsrapporten (alternativt räkneövningen) redan avhandlad. Sen. Igen.

Detta kandidatarbete handlar inte om komma försent till jobbet. Däremot handlar det på ett sätt om cyklar i motvind. För arbetstagare och studenter är inte de enda som kommer för sent när det blåser från fel håll: materiens små, små byggstenar kan ha liknande problem.

Den elektricitet som just nu gör det möjligt för dig att läsa det här (eller åtminstone hjälper till) består av en stor mängd små, elektriskt laddade partiklar som i en strid ström rusar genom kablarna från kraftverket in i ditt hem, din arbetsplats eller skola. Dessa partiklar, som kallas elektroner, är väldigt viktiga. De utgör inte bara grunden för det moderna samhället - de är även en av de centrala delarna utav de atomer som bygger upp all materia runtomkring oss. Där hålls de fångna av de så kallade atomkärnornas starka dragningskraft. Men med hjälp av till exempel en kraftfull laser kan man rycka bort elektronerna; man säger att atomerna joniseras. Detta i sig kan tyckas fascinerande, men om man ökar laserns styrka till oerhört höga nivåer kan verkligt underliga saker hända. Däribland just det fenomen som detta arbete tar avstamp i: atomerna kan fås att skicka ut extremt korta ljuspulser. Dessa pulser kan man använda till olika ändamål, bland annat för att jonisera en ny grupp av atomer. De elektroner man således rycker bort kommer till viss del ta över de korta ljuspulsernas speciella egenskaper. Om man dessutom låter en del av den första lasern samverka i denna senare jonisation så får man möjlighet att titta på mycket intressanta och väldigt specifika egenskaper gällande själva bortryckningen. För att göra detta på ett givande sätt måste man till väldigt hög noggrannhet kunna kontrollera skillnaden i sträcka som lasern färdas jämfört med de korta ljuspulserna. Om

vi för en stund antar att detta låter sig göras: vad är det då man tittar på?

För att förklara detta hjälper det oss att tänka på elektronerna man rycker bort som små, små cyklar. Små, små arbetstagare och skolelever som, när de väl har ryckts bort, cyklar febrilt bort från kärnorna. Men precis som en människa på väg till jobbet stöter de på problem. Faktum är att dessa elektroner kämpar mot en stark motvind: atomkärnornas dragningskraft! Denna motvind gör, som vi ju alla vet, att elektronerna kommer fram senare än vad de annars skulle ha gjort, och det är just denna förseningstid som man vill mäta, eftersom den säger en hel del om hur atomen i sig fungerar. Det visar sig nämligen att elektroner från olika atomer, och till och med olika delar av samma atom, blir olikt mycket försenade. Frågan blir således: hur mycket blåser det egentligen i olika atomer? Det är detta forskare världen över, och däribland i Lund, just nu jobbar hårt för att ta reda på. Att undersöka hur vindstyrkan skiljer sig från atom till atom är naturligtvis mycket intressant, eftersom det låter mänskligheten förstå grundläggande fakta om hur materien som bygger upp oss och allt annat faktiskt fungerar.

Men för att kunna göra allt detta behöver man som sagt kunna kontrollera och ställa in ett väldigt litet avstånd. Att exakt kunna mäta denna avståndsskillnad är inte helt lätt. Vad detta arbete handlar om är byggandet och testandet av en konstruktion av speglar som är tänkt att göra just detta: en så kallad interferometer. Denna interferometer använder sig bland annat av en specialbyggd spegel som här testas för första gången. I arbetet visar jag att den byggda interferometern gör vad den ska och därmed att den principiella designen fungerar. Samtidigt upptäcks en del konstigheter angående interferometerns stabilitet (en i sammanhanget såklart väldigt intressant egenskap). Ett slutgiltigt svar på anledningen till dessa problem hittas inte, men däremot har en hel del möjliga orsaker kunnat uteslutas och dessutom ger jag i slutet av arbetet en del förslag på hur man kan fortsätta söka efter källan. Men tack vare bekräftelsen att interferometerdesignen, inklusive den speciella spegeln, faktiskt fungerar kommer den nu att inlemmas i forskningsgruppens större uppställning för att till sist kunna användas för att mäta hur mycket det faktiskt "blåser" i atomer.

List of Abbreviations

APT	Attosecond Pulse Train
ATI	Above-Threshold Ionization
CCD	Charge-Coupled Device
CPA	Chirped-Pulse Amplification
CW	Continuous Wave
EWP	Electron Wave-Packet
HeNe	Helium-Neon
HHG	High-order Harmonics Generation
IR	Infra Red
LLC	Lund Laser Center
MI	Multiple Ionization
RABITT	Reconstruction of Attosecond Beating by Interference of Two-photon Transitions
VMIS	Velocity Map-Imaging Spectrometer
XUV	eXtreme Ultra-Violet

Contents

1 Introduction

Light has for a long time played a central role in the development of human society. As cinematography evolved from photography it quickly became obvious that light pulses of short duration were instrumental in the capture of rapid processes: a bright flash can be used to illuminate a moving target for a brief period of time, thus providing a snapshot of the object in movement. Several such snapshots in sequence form a movie of the captured process. Since the early 1900:s, great progress in the creation of short light pulses has been made, largely enabled by the invention of the laser in 1960. In the 1980:s, the Ti:Sapphire laser [1] in conjunction with a method called Chirped Pulse Amplification (CPA) [2] led to the availability of very short pulses (of femtosecond duration) of very high peak intensity (10^{14} W/cm^2). Pulses of this duration can be used to study e.g. molecular dynamics such as rotation and vibration.

The next step in the science of short pulses, into the attosecond ($1 \, \mathrm{as} = 10^{-18} \, \mathrm{s}$) regime, was taken not through new laser improvements but rather by the application of the existing Ti:Sapphire technology on an ensemble of atoms. The interaction of the very strong electromagnetic field provided by the Ti:Sapphire pulses with the atomic matter led to several new, non-linear phenomena being discovered: Multiple Ionization (MI), Above-Threshold Ionization (ATI) and High-order Harmonics Generation (HHG) [3][4]. Importantly, the process of HHG was found to result in the production of a sequence of extremely short (attosecond) pulses [4]: a so-called Attosecond Pulse Train (APT). Of equal significance is the frequency spectrum of an APT: it consists of a large number of distinct peaks centered at the odd harmonics of the central angular frequency ω_L of the laser used in the generation of the APT. The harmonics, remarkably, extend to very high orders (corresponding to eXtreme Ultra-Violet (XUV) radiation) before they drop in intensity, thus forming a frequency "plateau". The temporal properties of APT:s open up for time-resolved studies on the *atomic* scale, and the frequency characteristics allow for precision studies of e.g. the process of atomic ionization. These and similar studies thus represent the next step in the long scientific story of short light pulses.

The present study is part of a larger endeavor of attempting to ensure the stability, and thus feasibility, of long-term, high precision ionization dynamics experiments carried out by the division of Atomic Physics at Lund University at the Lund Laser Center (LLC). More specifically, the thesis centers on the construction and characterization of an optical interferometer intended for use in such attosecond experiments.

In the following the theory of HHG and relevant experimental applications thereof will be briefly presented to more deeply contextualize the thesis. From these considerations it will be possible to explicitly state the aim of the project at hand.

1.1 High-order Harmonics Generation

The process of HHG is commonly explained in terms of the semi-classical three step model, first presented by Corkum in 1993 [5]. This model considers how a single atom interacts with a strong external laser field. In the presence of field strengths on the order of 10^{14} W/cm^2, the Coulomb potential of the atom will be deformed (see figure 1), forming a potential barrier of finite width through which an atomic electron may tunnel (step 1). This process ionizes the atom and is known as tunnel ionization. This is of course a quantum mechanical effect, but subsequent to the ionization the electron is considered a classical, charged particle. Such an electron will be accelerated in the laser field and
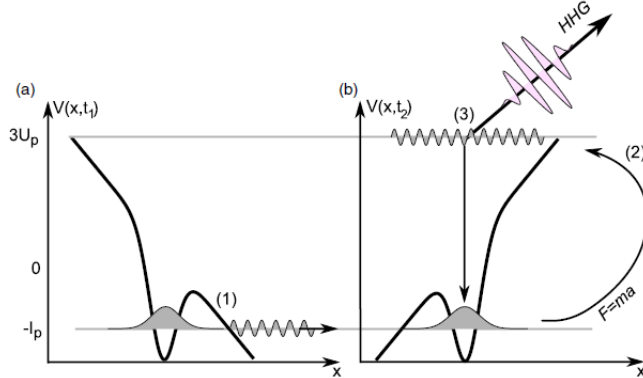
Figure 1: The semi-classical three step model of HHG. Adapted from [7]. (1): tunnel ionization of an atom in a strong ($\sim 10^{14}\,\text{W/cm}^2$) laser field. (2): the electron follows a classical trajectory in the laser field and (3) recombines with the parent atom, whereupon the excess energy garnered in the laser field is emitted as a short burst of light.

follow a specific trajectory (step 2) depending on when during the optical cycle of the laser it tunneled. When these classical trajectories are computed it is found that electrons tunneling during a specific time window (of length $T/4$) may be driven back to the parent atom, where they will recombine (step 3). This process repeats itself every half-cycle of the laser field. The time the electrons spend in the continuum is called the excursion time. Upon recombination, the energy the electron accumulated during the acceleration (plus the ionization potential energy I_P of the atom) will be emitted as electromagnetic radiation. An optimum excursion time corresponding to a maximum photon energy [5] of

$$\hbar\omega_c = I_P + 3.17 U_P \tag{1}$$

can be calculated. ω_c is the so-called cutoff frequency and U_P is the average energy of an electron in the oscillating electromagnetic field (called the ponderomotive energy). Excursion times longer or shorter than this optimum will correspond to lower electron energies; the "long" trajectories have a negative chirp and the short a positive chirp [6]. Due to the greater dispersion of the long trajectories, normally only the radiation generated by the short trajectories are used in experiments. At the Lund Laser Center, HHG is accomplished by firing a pulsed Ti:sapphire IR laser into a gas jet of argon (Ar) atoms synchronized with the laser. The Ti:sapphire laser typically has a pulse duration of about 25 fs, a pulse energy of 5 mJ, a repetition rate of 1 kHz and a central wavelength of $\lambda = 800\,\text{nm}$. For this λ, $T \approx 2.67\,\text{fs}$. This means two things: firstly, that for each pulse there will be approximately 20 half-cycles of high enough intensity for tunnel ionization to occur, and secondly, that the length of the radiation emission time window will be on the order of 100 as. As a consequence each pulse from the Ti:sapphire laser will generate a sequence of light pulses, each with attosecond duration: an Attosecond Pulse Train (APT) is formed. The APT will be phase-locked with the driving laser, i.e. they have a fixed phase-relationship, and co-propagate with it, due to the coherency of the emission process.

A single attosecond pulse considered by itself will consist of frequencies ranging from the fundamental frequency up to ω_c. However, the APT as a whole features as we have seen a temporally periodic structure with a pulse spacing of $T/2$. In the frequency domain this corresponds to a periodicity of $2\omega_L$. This indicates that the APT will consist of the

odd harmonics ($\omega_L + n2\omega_L \qquad n = 0, 1, 2, ...$) of the driving frequency only. This is strictly true only for an APT of infinite length and in reality the frequency spectrum will consist of peaks of a certain width centered at the odd harmonics. The peculiar frequency structure of APT:s is exploited to study atomic ionization dynamics in the measurement scheme called Reconstruction of Attosecond Beating by Interference of Two-photon Transitions (RABITT).

1.2   Electron Interferometry - RABITT

RABITT was first proposed by Müller in 2002 [8] as a method of characterizing APT:s. But the method can also be used to study the ionization dynamics of atoms [6] [7]. The accuracy of such measurements relies heavily on the ability to precisely control a phase delay between two laser beams. The phase delay is determined and monitored by study of an interference pattern formed by the two beams. Hence, a very stable interferometer setup is needed: as will be seen in the following discussion, the difference in interferometer arm length must be controllable to a fraction of the IR wavelength, i.e. on the nanometer scale. This corresponds to a time delay τ between the arms of much less than $T \approx 2.67\,\mathrm{fs}$. Naturally, this is a formidable challenge and clever schemes have to be employed to meet it. In the following, ionization using an APT is briefly introduced. Based on this discussion the implementation of RABITT will be explained.

Let us now consider an APT incident on an ensemble of atoms. If the harmonics extend to large enough frequencies (which they usually do), the APT will ionize the atoms. One quickly realizes that the ionized photoelectrons will have an energy distribution governed by the peculiar frequency structure of the pulse train. The electron energy spectrum will hence have distinct peaks at energies $\hbar\omega_e = \hbar\omega_q - I_P$, where ω_q is the frequency of the q:th harmonic. This energy spectrum can be measured using e.g. a Velocity Map Imaging Spectrometer (VMIS). RABITT exploits the wave-nature of the electrons and hence it will be useful to describe the photoelectrons in terms of a free Electron Wave Packet (EWP) in the following.

In RABITT, the above situation is manipulated to produce electron energy peaks in-between those described above, i.e. corresponding to the *even* harmonics of the driving laser. If the ionization is allowed to take place in the presence of an additional laser field (called the probe) the EWP may interact with this field, emitting or absorbing photons: the probe induces two-photon transitions. If the intensity of the probe is low enough this interaction will for all intents and purposes be limited to the emission or absorption of single photons. In RABITT this is exactly what is done, with the additional, low-intensity field being a fraction of the laser (of frequency ω_L) used for the generation of the APT (the pump). Since the frequency spacing of the APT is $2\omega_L$, it is clear that the emission or absorption of single photons of frequency ω_L will lead to the formation of sidebands at the even orders of ω_L in the electron energy spectrum. In fact, there are *two* possible (quantum) paths contributing to each sideband S_q. As depicted in figure 2a, this arises since an electron ionized by harmonic $(q-1)$ absorbing a probe photon will have the same final energy as an electron ionized by harmonic $(q+1)$ emitting a probe photon. Since each photon carries a certain phase (again we are considering a purely quantum mechanical effect) in addition to the different harmonics having different phases, it is clear that the phase accumulated by the EWP over the two paths to the same sideband differs. This leads naturally to an interference between the EWP:s traveling the respective paths and a subsequent modulation of the sideband intensity I_{S_q}. The phase difference between the
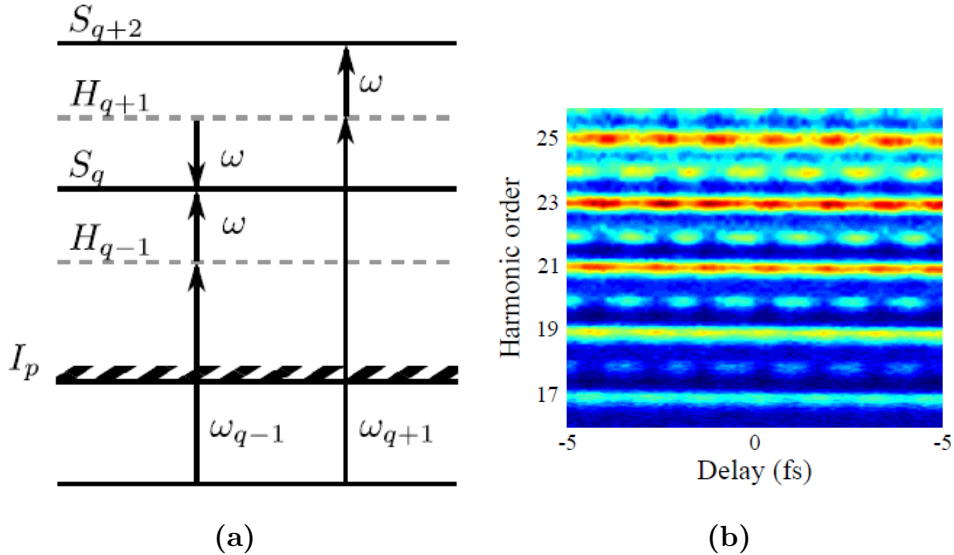
Figure 2: (a): The principle of RABITT. Atomic electron states are ionized by an APT consisting of odd harmonics ω_{q+i} of the IR pump frequency ω. The ionization takes place in the presence of a low-intensity IR probe of equal frequency, inducing two-photon transitions leading the the formation of sidebands S_q at even harmonics of the IR pump. Note that there are two possible quantum paths contributing to each sideband. (b): Typical RABITT-measurement result showing sideband modulation due to interference of the quantum paths depending on the delay τ between pump and probe. Figures adapted from [6].

pump and the probe will influence the interference as well. This phase difference can be described in terms of the (time) delay τ of one beam relative to the other. According to [4], the sideband intensity is thus proportional to

$$I_{S_q} \propto 1 + \cos(2\omega_L\tau - \Delta\phi_q - \Delta\phi_q^{at}) \tag{2}$$

where $\Delta\phi_q$ is the phase difference between the two harmonics contributing to the sideband in question. The term $\Delta\phi_q^{at}$ is the so-called atomic phase, which has yet to be introduced. Figure 2b shows a typical RABITT spectrogram, with the (even-order) sideband intensity modulation clearly visible as a function of τ. In a RABITT experiment, τ is controlled by changing the optical path length of the probe relative to the pump using a mirror mounted on a translation stage. By stepping through a range of τ-values, I_{S_q} can be measured.

In a traditional RABITT measurement $\Delta\phi_q^{at}$ is assumed to be small and subsequently ignored, allowing for $\Delta\phi_q$ to be determined. If $\Delta\phi_q$ and the amplitudes of each harmonic are known, the APT can be fully characterized [8]. If, however, the characteristics of the APT are known beforehand, the RABITT-scheme can be used to study the atomic phase $\Delta\phi_q^{at}$. $\Delta\phi_q^{at}$ is a phase delay partly introduced by the interaction of the ionized electron with the Coulomb potential of the parent atom [6]. Due to screening effects caused by the remaining electrons, it is expected that electrons ionized from different atomic subshells "see" different potentials. By measuring $\Delta\phi_q^{at}$ such theoretical predictions can in principle be tested quantitatively. This was done by e.g. Klünder *et al* [9], where the photoelectron time delays of the $3s^2$ and $3p^6$ shells in argon were investigated.

But since the absolute phases of the pump (or equivalently, the APT) and the probe are not known, $\Delta\phi_q^{at}$ cannot be determined directly. Instead, measurements on two different

systems (e.g. two different atoms) must be compared to derive the difference between the atomic phases of the two systems [10]. Clearly, this approach works only if the same experiment can be repeated twice with all other parameters equal. The main difficulty in this lies in ensuring that the phase delays in the two measurements are the same, which in turn requires a very robust way of determining τ. The standard method of doing this is to split off and overlap fractions of the pump and the probe and derive τ from the relative phase of the ensuing interference pattern.

By connecting the software determining τ to e.g. a piezo element controlling the delay via a feedback loop, the accuracy of the measurement can be increased since this setup allows for the stabilization of the delay in regards to variations caused by e.g. vibrations. The beams generating the interference pattern used for the stabilization are hence not the beams interacting in the RABITT-measurement. In this sense the delay is stabilized indirectly. Any asymmetry in the paths of the two pair of beams after the split-off thus opens up for the possibility that the delay stabilized for is not the same as that at the ionization target. Such a drift of the measured delay relative to the actual delay may be caused by the thermal expansion of one or more components not shared by the two pairs of beams. The issue of thermal expansion is made more severe as the components are contained in a vacuum environment, thus leaving the relatively inefficient process of thermal radiation as the only available cooling channel.

1.3 Aim and Motivation of the Thesis

Problems with drift most likely owing to such thermal expansion have been experienced at the setup for RABITT-measurements at the LLC [10]. In order to increase the long-term stability of measurements, thus enabling a higher signal-to-noise ratio, as well as guaranteeing good repeatability of experiments, it is of great interest to overcome these problems. A good way of doing this is to minimize the difference between the paths of the two pairs of beams. With this in mind a new interferometer design has been proposed within the research group. Using this design the beam path differences are reduced to the front- and backside of a custom-built, hole-drilled metallic mirror of very low thermal expansion coefficient. Hence, the proposed design should be less sensitive to delay drifts. The aim of this thesis is to construct and evaluate this setup.

The new design features a special method of determining the delay τ. As explained above this is usually done by interfering parts of the pump and probe beams. The new design instead features a low-energy, continuous wave (CW) laser which co-propagates with the pump and probe beams. The delay is then determined from the interference of this co-propagating beam with itself. A similar interferometer design was reported in 2009 by Chini *et al* [11].

A model of the new design has previously been evaluated using the ray-tracing software FRED with preliminary good results. The main aim of the thesis is to carry out the construction of the proposed setup in order to determine whether it actually produces an interference pattern of high enough quality. Granted that this phase of the endeavor is successful, the stability of said interference pattern should be evaluated. Naturally, an interferometer of greater intrinsic stability, e.g. less sensitive to environmental effects such as vibrations, will be easier to stabilize in RABITT-experiments, thus minimizing the risk of erroneous delay measurements. It is therefore of interest to characterize the stability of the delay as derived from the interference fringes produced by the co-propagating beam.

There are two limitations to this project: firstly that the construction will take place

off-line, in the sense that the only laser used will be the one intended for stabilization purposes (referred to as the co-propagating beam above). This limitation is acceptable since it still allows for a proof-of-principle evaluation of the setup. The second limitation is that the constructed prototype will not be an exact replica of the design as it is intended in the HHG beamline. The main difference is that an IR-absorbing and pulse-compressing aluminum-filter is not included in the constructed setup. The other difference is that the actual setup requires a more elaborate combination of mirrors to guide the stabilizing beams to the camera, due to the vacuum chambers surrounding that part of the HHG setup.

The aim of this thesis is thus two-fold: 1) to physically construct the interferometer setup to validate that it produces the expected interference pattern, and 2) to evaluate its stability.

This concludes the introductory part of the report. The next section will provide a theoretical description of optical interferometry, starting with a review of wave optics and ending by considering the type of interferometry employed in the constructed setup. Section 3 explains the full interferometer design and its various crucial components: most notably the recombination mirror. Section 4 describes the constructed setup and the construction process thereof. Section 5 details the different measurements performed as part of this thesis in the characterization of the setup, and section 6 presents and discusses the results of the different studies. The thesis finalizes with a summary of the work performed and the results obtained, and gives recommendations for future research on the topic.

2 Optical Interferometry

This section will cover the theoretical description of light necessary to understand the working principle of the interferometer. The laser source used in all experimental activities connected to this thesis was a single-frequency CW Helium-Neon (HeNe) laser. Hence it is sufficient to consider coherent and monochromatic light only. In the framework of wave optics a laser is in most cases modeled as a Gaussian beam; this section will therefore briefly review its derivation. In principle, the interference in question is then that of two Gaussian beams, but motivated through the Gaussian beam's phase-properties the situation will be reduced to the interference of two oblique plane waves. This is a valid approximation since the wavefront of the beam is flat close to its focus.

2.1 Wave Optics

In the following the basics of wave optics will be reviewed, focusing on the description of coherent and monochromatic light.

A wavefunction is any function $u(\vec{r}, t)$ at position $\vec{r}$ and time t such that

$$\nabla^2 u - \frac{1}{c^2} \frac{\partial^2 u}{\partial t^2} = 0 \tag{3}$$

where c is the speed of light in the medium of propagation. Equation 3 is termed the wave equation. The linearity of equation 3 is the basis of the so-called principle of superposition: if u_1 and u_2 both satisfy equation 3 then so does $u = u_1 + u_2$.

Usually $u(\vec{r}, t)$ is described by a complex wavefunction $U(\vec{r}, t)$. For monochromatic light

$$U(\vec{r}, t) = U(\vec{r})e^{i2\pi\nu t} \tag{4}$$

where ν is the frequency of the wave and $U(\vec{r})$ its complex amplitude:

$$U(\vec{r}) = a(\vec{r})e^{i\phi(\vec{r})} \tag{5}$$

where $a(\vec{r})$ is the amplitude of the wave and $\phi(\vec{r})$ its phase. The wavefronts of a wave are defined to be the surfaces on which $\phi(\vec{r})$ is constant.

Analogous with equation 3, the complex amplitude has to fulfill the so-called Helmholtz equation

$$\nabla^2 U + k^2 U = 0 \tag{6}$$

where $k = \frac{2\pi\nu}{c}$ is called the wavenumber. The plane wave is a solution to 6 with a complex amplitude of

$$U(\vec{r}) = Ae^{-i\vec{k}\vec{r}} \tag{7}$$

where the constant A is called the complex envelope and $\vec{k} = (k_x, k_y, k_z)$ the wavevector. A property characteristic of the plane wave is that its wavefronts form parallel planes (hence its name), with $\vec{k}$ being normal to these. The wavelength λ of the wave is defined to be the distance between two consecutive wavefronts:

$$\lambda = \frac{2\pi}{k} = \frac{c}{\nu} \tag{8}$$

If the complex envelope of a plane wave is modified so as to vary slowly (compared to λ) with position, i.e. $A = A(\vec{r})$, the wavefront normals of the resulting wave will form paraxial rays. Hence a plane wave modulated in this way is said to be a paraxial wave. The complex amplitude of a paraxial wave is thus

$$U(\vec{r}) = A(\vec{r})e^{-i\vec{k}\vec{r}} \tag{9}$$

A substitution of equation 9 into 6 in conjunction with the approximation of neglecting $\frac{\partial^2 A}{\partial z^2}$, yields the following condition (called the paraxial Helmholtz equation) for the complex envelope

$$\nabla_T^2 - i2k\frac{\partial A}{\partial z} = 0 \tag{10}$$

where $\nabla_T^2 = \frac{\partial^2}{\partial x^2} + \frac{\partial^2}{\partial y^2}$. Now we finally arrive at the Gaussian beam, as one of the solutions to 10.

2.2 The Gaussian Beam

A Gaussian beam traveling along the z-axis can be described using a set of two coordinates: the axial position z and the radial position ρ. The beam center is localized at $z = \rho = 0$. The beam has its maximum intensity on the beam axis; the intensity of the beam follows a Gaussian distribution centered on the beam axis, decreasing as ρ increases. $z = 0$ is

the point at which the width of the transverse intensity distribution is the smallest (the "waist" of the beam). The function $W(z)$ describes the width of the beam along the z-axis and thus assumes its minimum value at precisely $W(z=0) = W_0$. Hence W_0 is known as the waist radius.

We will now consider the properties of the Gaussian beam related to its phase and wavefronts. The phase of a Gaussian beam is given by

$$\phi(\rho, z) = kz - \zeta(z) + \frac{k\rho^2}{2R(z)} \tag{11}$$

where

$$\zeta(z) = \tan^{-1}\left(\frac{z}{z_0}\right) \tag{12}$$

and

$$R(z) = z\left(1 + \left(\frac{z_0}{z}\right)^2\right), \tag{13}$$

where the constant z_0 is labeled the Rayleigh range of the beam. $\zeta(z)$ describes the phase retardation that a Gaussian beam exhibits relative to the phase of a plane wave: the Gouy effect (as is evident from equation 7 kz is the phase of a plane wave traveling in the z-direction). The maximum magnitude of the Gouy effect is π. z_0 can e.g. be defined as the axial distance at which $\zeta(z) = \frac{\pi}{4}$. The other function important in describing the phase of a Gaussian beam is $R(z)$: the on-axis wavefront radius of curvature. It will be instructive to consider a few limiting cases of $R(z)$: at the beam center $R(z=0) = \infty$ and the wavefronts are planar; greatest curvature is achieved at $z = z_0$; for $z \gg z_0$, $R(z) \approx z$ and the wavefronts have approximately spherical curvature. The term $\frac{k\rho^2}{2R(z)}$ describes then deviations of the phase from the behavior described by $R(z)$, at off-axis positions. For small ρ this deviation will be minimal and we thus find that a Gaussian beam can be approximated by a plane wave near its beam center, i.e. for small z and ρ. Based on this approximation we will solely consider the interference of plane waves and assume that this treatment holds equally well for the laser beam to be used in the interferometer.

This approximation will be of great use when we discuss the interference of Gaussian beams in the following section.

2.3 Interference

Interference is the general concept of intensity modulation due to the superposition of two or more waves. Since the intensity of a wave is the square of its (complex) amplitude, the resulting intensity as a function of position of two superposed monochromatic plane waves with complex amplitudes $U_1(\vec{r}) = A_1 e^{i\phi_1} = \sqrt{I_1}e^{i\phi_1}$ and $U_2(\vec{r}) = \sqrt{I_2}e^{i\phi_2}$ will be

$$I = |U_1 + U_2|^2 = |U_1|^2 + |U_2|^2 + U_1^*U_2 + U_1 U_2^* \tag{14}$$

$$= I_1 + I_2 + \sqrt{I_1 I_2}e^{-i(\phi_1 - \phi_2)} + \sqrt{I_1 I_2}e^{i(\phi_1 - \phi_2)} \tag{15}$$

$$= I_1 + I_2 + 2\sqrt{I_1 I_2}\cos(\phi_1 - \phi_2) \tag{16}$$

From this it is obvious that the resulting intensity will vary as a function of the phase difference $\Delta\phi = \phi_1 - \phi_2$; it will be maximum for $\Delta\phi = 0, 2\pi, ...$ and minimum for $\Delta\phi = \frac{\pi}{2}, \frac{3\pi}{2}, ...$ Since the phase of monochromatic waves is a function of $\vec{k} \cdot \vec{r}$, it is possible to introduce

a phase difference by varying $\vec{r}$. A difference in $\vec{r}$ can be achieved by delaying one of the waves relative to the other (this is done in e.g. Mach-Zehnder or Michelson interferometers). Alternatively two waves of different directions of propagation may be superposed to create a phase difference. This is the method employed in the constructed interferometer setup and the next section will be devoted to its explanation and description.

2.3.1   Oblique Interference

We will now consider two monochromatic plane waves with complex amplitudes U_1 and U_2 respectively. We assume that wave U_1 propagates along the z-axis, i.e. that

$$U_1 = \sqrt{I_1}e^{-ikz} \tag{17}$$

and that wave U_2 travels in the x-z plane at an angle θ to U_1:

$$U_2 = \sqrt{I_2}e^{-ik(z\cos\theta + x\sin\theta)}. \tag{18}$$

Assuming that we are detecting the interference in a plane perpendicular to the wave U_1 (i.e. the x-y plane), $z = 0$ and the phase difference between the two waves will be $\Delta\phi = kx\sin\theta$. According to equation 16 the resulting intensity distribution is given by:

$$I = I_1 + I_2 + 2\sqrt{I_1 I_2}\cos(kx\sin\theta). \tag{19}$$

From this it is clear that the interference pattern will be sinusoidally distributed along the x-axis with period $\frac{2\pi}{k\sin\theta} = \frac{\lambda}{\sin\theta}$. If we make the restriction $\theta \in [0, \frac{\pi}{2}]$, we will have that a small θ, and hence small $\sin\theta$, corresponds to large period. Thus small angle oblique interference will generate a pattern containing fewer fringes in a given section than if a larger angle had been used.

As has already been stated, oblique interference forms the theoretical basis of the interferometry in the setup to be constructed. In the setup, two parallel, divergent beams will be sent through a focusing lens. Since the beams are divergent, they will start to overlap even before they reach the focus of the lens. As described in this section, two beams overlapping in this way will give rise to an interference pattern. This pattern can then be detected by a camera and, as will be explained in further detail later, used for the active stabilization of the interferometer. The next section will give an overview of the interferometer design, thus explaining how this interferometric situation is brought about.

3   The Interferometer Design

The interferometer is of the Mach-Zehnder type and features two arms, starting at a beamsplitter and ending at the recombination mirror. The beamsplitter splits an incoming laser beam by transmitting 70% and reflecting 30%. In the design, the pulsed IR laser and the HeNe beam enter the setup according to figure 3. In the case of the HeNe, the transmission enters into the pump arm and the reflection into the probe arm of the interferometer. In both arms the beam is focused by a 2" focusing mirror, into which it is guided by a regular 2" mirror (figure 7 details the constructed setup). In the proposed design, the focal length of the probe mirror is 650 mm and 750 mm for the pump. The intensity of the focused pump IR beam is high enough to induce ionization in air, wherefore

it has to enter a vacuum environment not too long after the focusing mirror; the same is of course true for the IR probe.

In the actual setup, the gas target for harmonics generation would be placed in the pump arm focus. The generated APT would then co-propagate with both the IR pump laser and the HeNe passing first a pair of silica-plates and then a thin aluminum foil. The role of both these components is to remove as much of the IR pump beam as possible. The silica-plates are Anti-Reflection (AR) coated for 800 nm and thus the majority of the IR pump would be transmitted through the first plate, while the APT and the HeNe are reflected according to figure 4. Thus the geometry of the plate-pair allows for the separation of the IR pump from the two other beams. The Al-foil has high absorbance in the IR region but will let the XUV APT pass through with minimum loss of intensity. Different types of metallic foils can be used, e.g. allowing for the selection of specific harmonics. These foils are often very delicate, and the silica-plates have been introduced to reduce the wear on them. In addition to absorbing the IR, the Al-foil compresses the as-pulses temporally. Due to the absorbance of the Al-foil, the HeNe beam must be large enough to pass around it. Naturally, this sets some requirements on the mounting of the foil. After passing these components, the pulse train and the now annular HeNe beam reach the recombination mirror (more of which anon).

Meanwhile, the IR probe beam co-propagates with the HeNe in the probe arm. The interferometer design features two translation stages in the probe arm: one before the focusing mirror and one directly after it. The first stage allows for the coarse adjustment of the relative interferometer arm length. A piezo-controlled translation stage is mounted on top of the second stage, and a retroreflector is in turn mounted on the piezo stage. The second stage thus allows for both the fine adjustment of the probe focal point as imaged in the spectrometer, and for the control and stabilization of the delay τ between the APT and the probe by shifts of the retroreflector using the piezo stage. The piezo element is governed via the software analyzing the interference pattern (this will be discussed in more detail soon). After passing these components the two beams are guided to the recombination mirror.
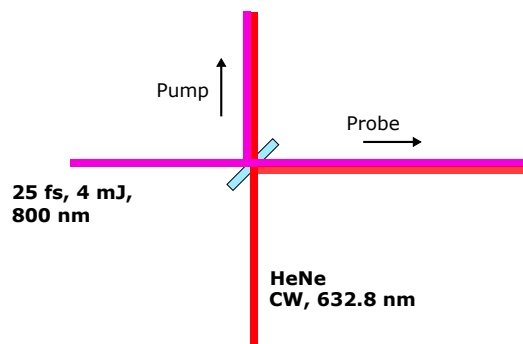

Figure 3: Schematic illustration of the orientation of the incident lasers on the beamsplitter in the interferometer design: the pulsed IR laser enters from the left in the figure and the co-propagating HeNe beam from the bottom. "Pump" and "Probe" denote the pump and probe arm of the interferometer, respectively.
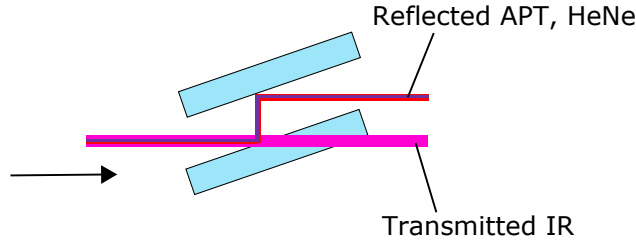
Figure 4: Working principle of the silica-plates in the pump arm of the interferometer. The IR beam is transmitted, while the APT and the HeNe laser are reflected.

3.1   The Recombination Mirror

The recombination mirror is the centerpiece of the interferometer design. It is a silver coated 1" (25.4 mm)-mirror through which two perpendicular channels have been drilled. The mirror substrate is made from the material Zerodur, which has a very small thermal expansion coefficient (see [12] for specifications). The channels meet at one side of the mirror. Please see appendix A for further details regarding the mirror geometry. In figure 5 the mirror is depicted schematically in its intended use in RABITT experiments. The beams from the pump arm (APT and annular HeNe) enter from the left in the figure, and those from the probe arm (IR probe and HeNe) from the bottom. The APT passes straight through one of the channels in the mirror and exits the mirror surrounded by the majority of the IR probe, which has been reflected to form an annular beam. These beams are then guided to the ionization target of the RABITT experiment (this side of the mirror is for convenience referred to as the "detector-side" in the following). However, the central part of the probe beam passes through the other mirror channel and leaves the mirror parallel with the annular HeNe beam, which has been reflected on the mirror. These beams are guided to a focusing lens. Since the beams hit the lens at different positions, they will propagate towards its focus at a certain angle to each other. Furthermore, since they have passed the foci of the two focusing mirrors, the beams are at this point divergent. Hence they will begin to overlap before they reach the lens focal point, generating an interference pattern according to section 2.3.1. This interference pattern is detected by a CCD camera and analyzed by the detection software in terms of spatial frequencies. The software monitors how the phase of the pattern changes (i.e. how much the fringes move). With knowledge of the laser wavelength, this phase change can be converted to the corresponding shift in delay τ between the pump and the probe, or, equivalently, the shift of optical path-length responsible for the phase change. By coupling the software to the probe arm piezo element, this shift can be mitigated by moving the retroreflector an equal but opposite distance. The interferometer is then said to be actively stabilized.

There is, however, a certain difficulty connected with the detection of the interference pattern: due to the geometry of the recombination mirror, part of the IR probe is carried along to the camera. In order for the design to work as intended it must therefore be possible to separate the IR beam from the HeNe, since the comparatively high IR intensity would easily burn the CCD chip of the camera. But since the HeNe only was used in the constructed prototype, such precautions were not necessitated.
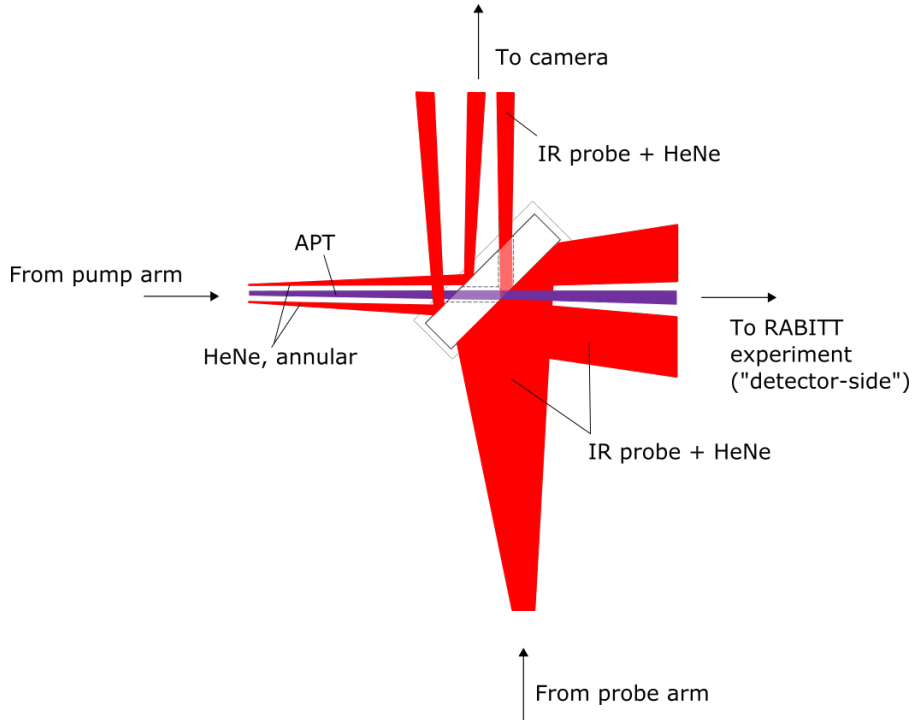
Figure 5: Working principle of the recombination mirror in use in a RABITT experiment. The APT and the annular HeNe beam enter from the left, and the IR probe and HeNe beam from the bottom. The beams exiting from the top are overlapped using a lens. A CCD camera is used to detect the ensuing interference pattern. The beams exiting to the right (APT and IR probe) are guided to the RABITT experiment ionization target.

3.2 Predictions

Two different simulations based on the FRED-model of the interferometer provided preliminary insight into the properties of the setup. Figure 6 shows interference fringes detected by the camera in a simulation by David Kroon.

Simon Ek, at the time of writing a fellow bachelor student in the research group, had as part of his thesis used FRED to study how angular drift of the HeNe beam would affect the measured delay. The relation was found to be linear with a proportionality factor of

$$k = 8.1704\,\text{fs/mrad}, \tag{20}$$

quoted here with Ek's permission. These simulations were done based on the design presented above, with $f_1 = 750\,\text{mm}$ and $f_2 = 650\,\text{mm}$ for the pump and probe focusing mirrors respectively. This and previous sections summarize the state of knowledge prior to the construction of the interferometer.

4 Construction of the Interferometer

This section will outline the construction process of the setup described above. The constructed setup differs from the description given above in three aspects: the probe arm focusing mirror has a different focal length (500 mm) and the Al-filter was not included, due to the risk of damage and deterioration due to oxidization. Lastly the setup constructed did not include the components necessary for its active stabilization. The
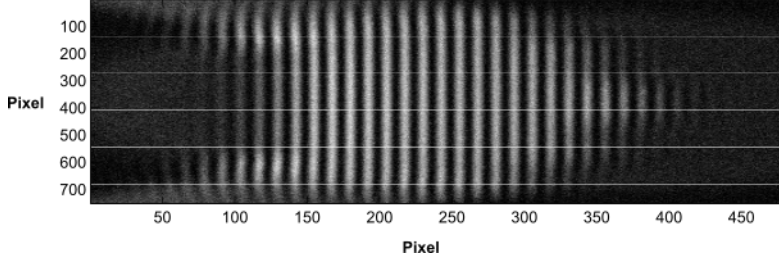
Figure 6: Simulated interference fringes based on the FRED-model of the interferometer, indicating the theoretical success of the design. Courtesy of David Kroon.

construction of the interferometer was carried out by the author during the first months of the year 2015 on an optical table in the "Kiloherz lab" at LLC. The majority of clamps, posts and mounts used were products from Thorlabs, the exception being the recombination mirror which was custom manufactured by EKSMA. The laser used was a 4 mW CW Helium-Neon laser (JDSU Model Novette^{TM} Series, see [13] for further information).

Prior to the construction there were a few technical issues which provided interesting questions regarding the feasibility of the design at hand. The backside of the beamsplitter that would be used in the setup was not AR coated for the HeNe wavelength (632.8 nm). Hence a part of the beam reflected by the beamsplitter would undergo multiple internal reflections, effectively rendering the beamsplitter a Fabry-Pérot etalon and introducing interference fringes in the probe arm beam. At the start of the thesis work it was unknown how much this "etalon-effect" would affect the beam quality, although ray-tracing simulations had indicated that the interference pattern used for delay stabilization would be severely distorted. Another possible issue concerned the mounting of the recombination mirror: the RABITT measurements require that the APT and the probe are collinear when they reach the ionization target. It is therefore vital that it is possible to align the recombination mirror such that the beams exiting on the detector-side are collinear while those exiting on the camera-side form vertical interference fringes (in order for the pattern to be interpretable by the detection software). At the start of the construction process it was not known whether a normal mirror mount would suffice for this, or if a gimbal-mount (which allows for rotation without translation) was required. The quality of the recombination mirror was a third issue. The mirror was custom built for this specific setup and hence it was unclear how smooth the drilled holes would be and in turn to what extent imperfect hole edges would affect the beam quality.

The diameter of the beam provided by the laser was 0.48 mm (see [13]) and with the recombination mirror hole diameter being 2.5 mm (see appendix A) it was clear that a beamexpander had to be used. The first step in the construction process was thus to build the beamexpander, which works along the principles of a Keplerian telescope and consists of two focusing lenses separated by the sum of their focal lengths. A collimated beam passing through both lenses will thus be magnified by a factor $M = f_2/f_1$, where f_1 and f_2 are the focal lengths of the first and second lens respectively. A number of different combinations of lenses were tested until $f_1 = +6$ mm and $f_2 = +125$ mm were finally chosen, thus giving a magnification of $M = 125/6 \approx 21$ and a final beam diameter of ~ 10 mm. The beam exiting the beamexpander was ensured to be collimated by observing how well a pattern cut in a piece of paper inserted in the beam overlapped with an identical pattern further down the beam, and adjusting the lens separation accordingly. After collimation, the beam was ensured to be level with the optical table. This was done by iteratively centering the beam on one of two apertures of the same height using the

two mirrors before the beamsplitter (see figure 7), until the beam was eventually centered on both apertures simultaneously.

Once the beam was collimated and at constant height the remaining optical components could be mounted and fastened to the table. No major difficulties were encountered during this part of the process except that a $f = 500\,\text{mm}$ focusing mirror (FM2 in figure 7) was used instead of the planned $f = 650\,\text{mm}$-mirror, since the delivery of the latter was delayed. As a consequence of this change the final setup attained a slightly more compact design since the components in the relevant interferometer arm had to be shifted to accommodate the change of focal length.

The recombination mirror was mounted in a 1" to 2" adapter which in turn was mounted in an ordinary mirror mount and placed at the crossing point of the beams. Using the adjustment screws on the mirror mount the two beams on the RABITT-side were made collinear. The collinearity could be confirmed by the formation of a concentric circular interference pattern on a screen beyond camera position 2 (C2, see figure 7). By symmetry, the two beams exiting the mirror on the opposite side were then parallel. Using a 1" mirror these two beams were guided into a focusing lens of $f = +1000\,\text{mm}$. This lens, as described in section 3, will cross the beams and thus give rise to an interference pattern detectable at C1.

Figure 7 shows the final version of the setup schematically and approximately to scale. The true distances are shown in mm. The HeNe laser beam is shown in red. The component labeled BS is the 70/30 beamsplitter. The focusing mirror FM1 has a focal length of $f = 750\,\text{mm}$ and FM2 $f = 500\,\text{mm}$. The black, tilted lines indicate Ag-coated mirrors, of which two (slightly longer and positioned before the focusing mirrors) are 2" in diameter and the rest are 1". TS denotes the translation stage, SP the silica-plates and RM the recombination mirror (please refer to figure 5 for a more detailed view). C1 and C2 indicate the two camera positions that were used in the measurements, although only one camera was used. Figure 8 show a few photographs of the finished interferometer.

This concludes the description of the construction process of the interferometer setup. In the following section the different measurements that were carried out on the setup will be described and motivated.

5   Measurements

The experimental measurements carried out in connection to the thesis can be divided into three phases: 1) beam studies, 2) delay stability measurements, and 3) pointing stability characterization. The camera used for all of the measurements was a Point Grey Firefly MV 1394a-model, connected via FireWire to a computer in proximity to the optical table. Various detection software was installed on the computer. The maximum framerate of the camera was 15 fps, though it at times briefly decreased to 8 fps.

5.1   Beam Studies

Directly after the construction of the interferometer was completed, the camera was placed in position C1 (see figure 7). A simple program was used to grab pictures from the camera video stream to study the interference pattern quality, as well as that of the individual beams. Two of the three delivered recombination mirrors were tested and were found to perform equally well.
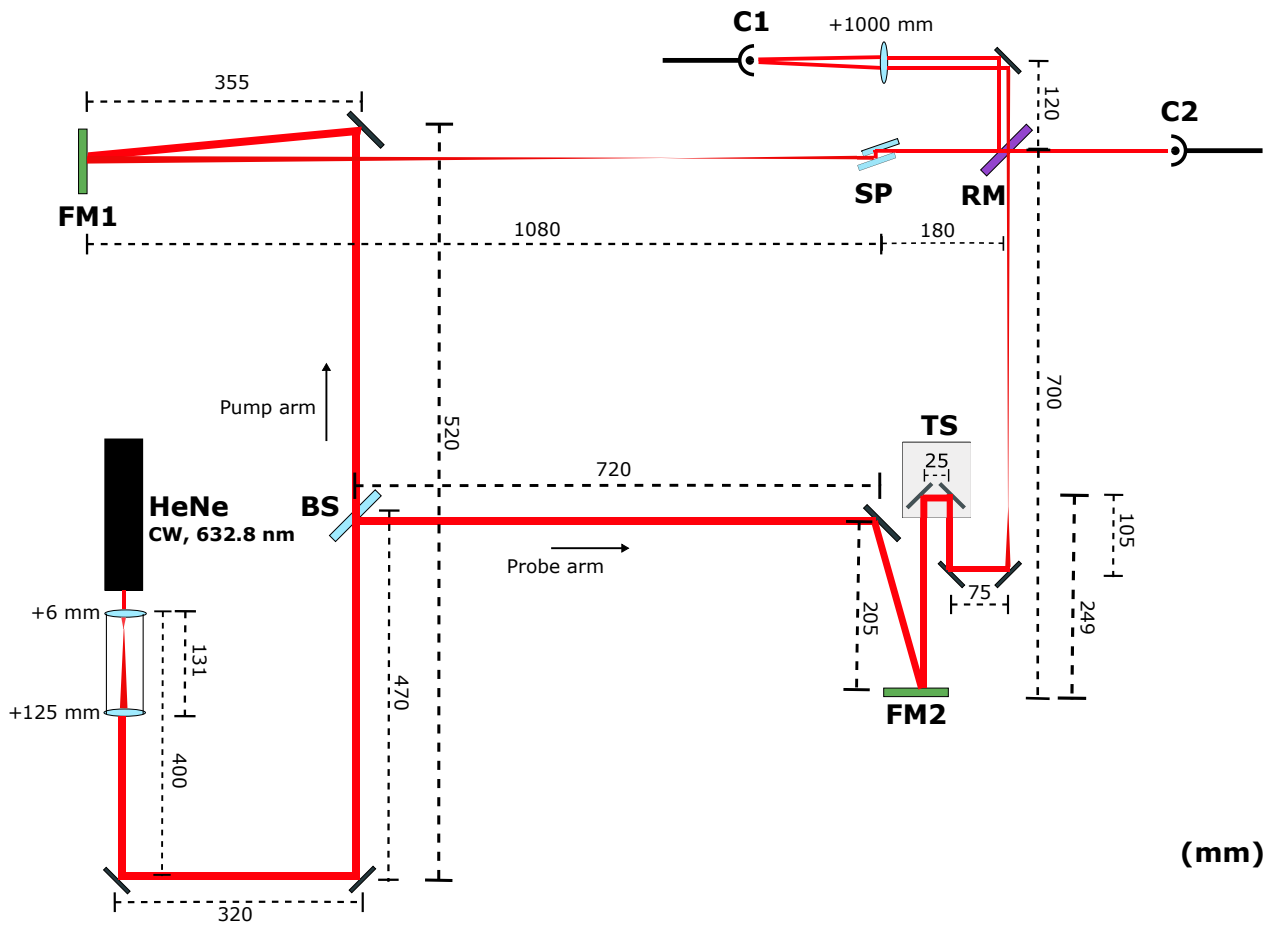
Figure 7: A schematic view of the constructed interferometer. All distances in mm. The HeNe laser beam is shown in red. BS = 70/30 beamsplitter. FM1 = focusing mirror 1 ($f = 750\,\mathrm{mm}$). FM2 = focusing mirror 2 ($f = 500\,\mathrm{mm}$). TS = translation stage. SP = silica-plates. RM = recombination mirror. C1, C2 = camera positions 1 and 2.
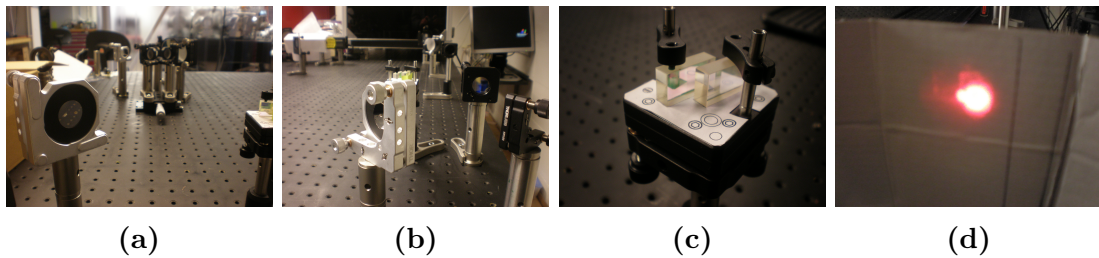

Figure 8: Photographs of parts of the experimental setup. (a): The mounted recombination mirror, with the translation stage in the background. (b): The recombination mirror from the other side. Also seen is the lens used to overlap the beams, and the camera in position C1 beyond the lens. (c): The silica-plates. (d): The laser beams at C1; the transmitted beam is starting to overlap with the annular. The picture is overexposed and the ring of the annular beam is thus not visible.

15

5.2 Delay Stability Measurements

A pre-existing, home-built LabView script was provided for the delay stability measurements. Using this script the camera video stream was analyzed in terms of (vertical) spatial frequency. In the resulting Fourier spectrum the peak corresponding to the interference pattern arising from the interference of the two beams could be selected. The initial position of that peak was assumed to correspond to a delay $\tau = 0$ (see section 1.2 for a discussion of the consequences of the delay relativity). The software then monitored and recorded the variation of the peak position in terms of delay. These measurements were carried out with the camera in both position C1 and C2. By "misaligning" the recombination mirror, vertical interference fringes could be obtained at C2. Several delay stability measurements were performed by the author, with lengths varying between 1 and 48 hours.

5.3 Pointing Stability Characterization

Several measurements were done to characterize the (angular) pointing stability of the HeNe laser. To this effect the two setups shown in figures 9a and 9b respectively were used, with the camera placed in the focus of the lens. As is apparent from these figures both the pointing stability of the beam with and without the expander was tested. In addition, the measurement modality depicted in 9b was used with no lens at all. The majority of the pointing stability measurements spanned 12 hours with a time-resolution of 60 s.

The detection software used in these measurements grabbed a frame from the camera feed at a set frequency and output a movie made up of these frames as an .AVI-file. Using a MATLAB-script originally provided by the supervisor and later modified by the author, the center-of-mass of each frame was computed to study the change of beam position as a function of time. Since the distance from lens to camera was known the corresponding angular shift of the laser could be calculated by trigonometry. Finally, the theoretical conversion factor, equation 20, allowed for the translation of angular shift to corresponding changes in measured delay. It is important to note that the constructed design from which these measurements originate differs from the design on which the simulations were based, in that FM2 has $f = 500\,\mathrm{mm}$ instead of $650\,\mathrm{mm}$. As a consequence, the effect of moving the beam across the mirror will not be exactly the same, due to the difference in mirror curvature. But when considering that a delay shift of e.g. $100\,\mathrm{as}$ corresponds to a change of relative path length of $30\,\mathrm{nm}$, it is clear that the relevant distances are on such a scale that the difference between the two mirrors is negligible. Thus the simulation results should still be accurate to a high degree.

The background subtraction employed in the analysis of the .AVI-files deserves a quick note. From inspection of individual frames it was found that the background noise level never exceeded a specific value. Thus the background could easily be subtracted. If instead a ratio to the max intensity had been used for background level determination, the background reduction would vary with intensity from frame to frame and change the beam profile. This would have induced errors in the position determination.
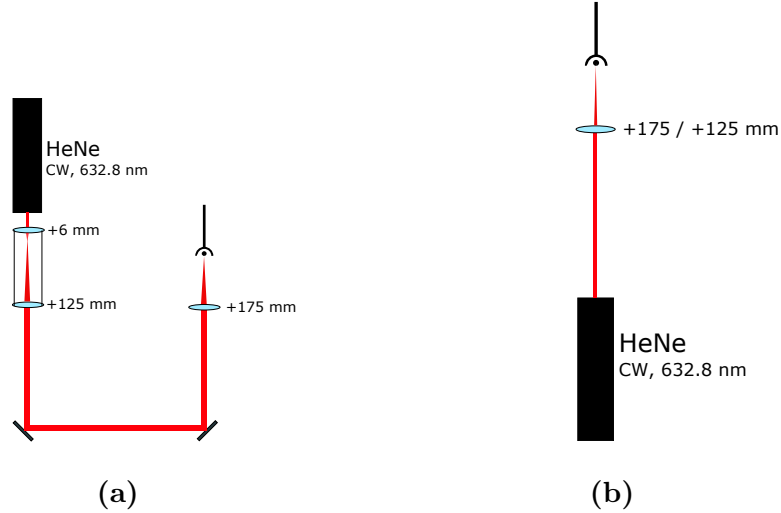
Figure 9: A schematic view of the setup for pointing stability measurements with, (a), and without, (b), the beamexpander.

6 Results and Discussion

In this section the main results of the measurements detailed in section 5 are presented. Because of the interdependence of the different measurements carried out, the results are discussed as they are presented.

6.1 Beam Studies

The following results were all obtained with the camera in position C1 and the setup as depicted in figure 7, with the beams exiting on the RABITT-side (C2) being collinear.

Figure 10a was obtained with the pump arm of the interferometer blocked and thus shows the beam transmitted through the recombination mirror only. The beam profile is far from clean and contains multiple diffraction artifacts. Conversely, the picture in figure 10b was taken with the probe arm blocked and shows the central part of the beam from the pump arm; this is the supposedly annular beam. As is readily seen, the central part of the beam is far from empty and encompasses a complex structure. The majority of the intensity lies, however, still in the annular part of the beam, as figure 10c shows. The beam artifacts depicted in the figures did not appear in either of the arms before the recombination mirror and can thus safely be said to originate from the mirror.

Finally, figure 11 was taken with both arms unblocked. The picture was taken at a distance from the lens such that the transmitted beam overlapped with the annular part of the reflected beam. Interference fringes are clearly visible, showing that the interferometer is capable of producing the expected interference pattern even though the transmitted and reflected beams are heavily distorted. Furthermore, the fringes are near-vertical, confirming that a regular mirror mount suffices for the alignment of the recombination mirror.

Figure 12 shows the probe beam after it has been reflected on the beamsplitter, photographed with a regular camera. The result of the etalon-effect discussed in section 4 is evident as a major vertical interference fringe. By adjusting the angle of the beamsplitter the position of the interference fringe relative to the beam center could be changed so as to not affect the measurements.
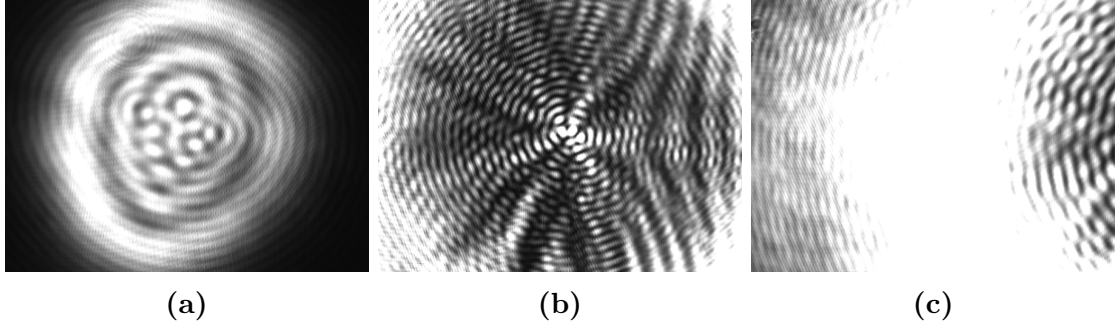
Figure 10: Beam studies at camera position C1. HeNe beam transmitted through the recombination mirror: (a). Center, (b), and side, (c), of the annular HeNe beam reflected on the recombination mirror.
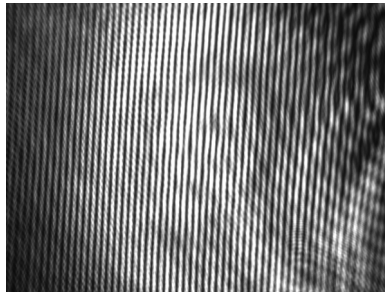

Figure 11: Interference pattern detected at camera position C1, indicating the success of the design.

6.2 Delay Stability Measurements

With the basic functionality of the interferometer design confirmed, the next step was to characterize the stability of the generated interference pattern. These results are expressed in terms of the actual time delay τ as explained in section 5.2. At the start of each measurement, τ was set to zero; for a perfectly stable interferometer setup the actual delay would remain at this value over time. As we shall see, the setup at hand is not perfectly stable.

The results of the delay stability measurements feature several distinct and recurring effects: a high-frequency stochastic variation of the delay ($\sigma \approx 0.85\,\mathrm{fs}$), sudden jumps in the measured delay of 2-4 fs, and oscillations with period ~ 1 hour and amplitude 3-5 fs. Typical examples of these characteristic features are shown in figures 13, 14 and 15. In addition, a long term drift of the measured delay was observed, exemplified in figure 16 which shows the result of a measurement with the camera in position C1. The actual delay after 41 hours was approximately $-70\,\mathrm{fs}$. The accumulated delay drift is partly a long term consequence of the sudden jumps and the oscillations, but as figure 15 shows, a linear slope superimposed on the other effects could be observed at some instances. The slope in this specific figure corresponds to a rate of change of $\sim 1.6\,\mathrm{fs/h}$. This is a typical value for those instances where a distinct slope is visible over several hours. The results also include slopes up to 6 fs/h or somewhat larger, but then during 0.5 hour at a time only. There are even examples of time intervals where no linear drift is present at all. It is therefore not possible to characterize a distinct linear drift based on the measurements.

The measurements conducted at C2 showed the same features with similar characteristics, although the sudden jumps seemed to be more frequent.

Figure 12: The probe beam imaged on a piece of cardboard just after the beamsplitter. A large interference fringe owing to the etalon-effect of the beamsplitter is visible, splitting the beam.
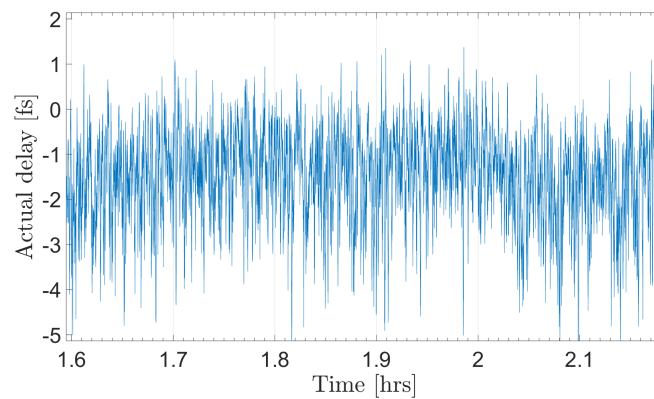

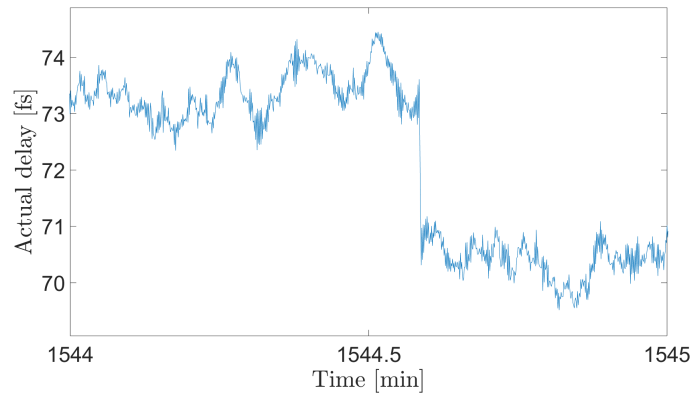**Figure 13:** Example of stochastic variations in the measured delay with a standard deviation of $\sim 0.85\,\mathrm{fs}$.

Figure 14: Example of a "sudden jump" with a typical magnitude of $\sim 3\,\mathrm{fs}$.

In order to better characterize and improve the interferometer it is important to seek the causes of these effects. The stochastic variation is most likely due to environmental, mechanical vibrations in the vicinity of the optical table, caused by e.g. vacuum pumps. Part of these variations is of course also attributable to detector noise. An early hypothesis to the cause of the sudden jumps was tension suddenly released in the translation stage mechanism. This possibility was however easily ruled out as delay measurements with the two mirrors previously mounted on the translation stage (see figure 7) fastened instead
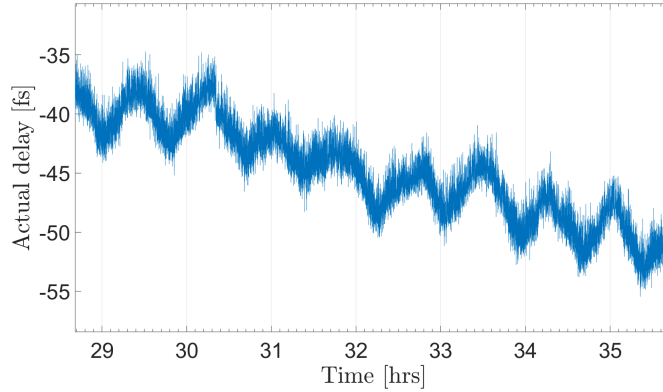
Figure 15: Example of oscillations in the measured delay of ~ 1 hour periodicity and $\sim 4\,\mathrm{fs}$ amplitude. Note the net slope of the oscillations, approximately corresponding to a drift of $-1.6\,\mathrm{fs/h}$.
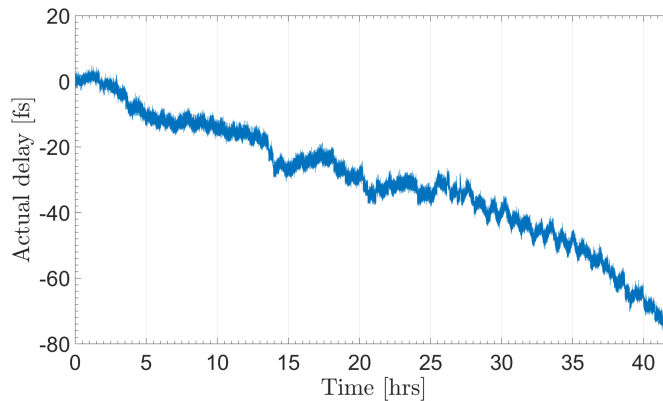

Figure 16: Typical long term delay stability measurement. The measurement was conducted with the camera at position C1 (see figure 7). The graph shows rapid fluctuations in delay, sudden jumps and oscillations. A linear drift can be seen in the graph, but its magnitude varies. An example of one of the instances is shown in figure 15.

directly to the optical table still showed similar sudden jumps. That the jumps might be caused by human activity (e.g. the closing of doors) could be excluded as the results show jumps more or less evenly distributed throughout several 24-hour periods. Neither the cause of the oscillations nor the tentatively observed drift was immediately obvious.

Hence, the final phase of measurements was aimed at finding an explanation to these effects. As a possible origin the HeNe laser itself was proposed: the hypothesis being that the laser pointing direction might vary so as to cause some or all of the unexplained effects. The connection between pointing stability and observed delay had of course already been shown by Ek (see equation 20). Hence, the question was rather one of magnitude and behavior.

6.3   Pointing Stability Characterization

The pointing stability of the laser was studied in two principally different modalities: with the beam passing through the beamexpander, and with it entering directly into the camera (see section 5.3). The results are presented as the change in delay τ as a function

of time, according to the same section.

6.3.1 With Beamexpander

Figure 9a depicts the setup from which these results originate. Two measurements, each spanning 12 hours were made, with a time resolution of 1 min. Figure 17 shows the first of these, with calculated delay drift as a function of time. The net delay drift after 12 hours is almost 1.6 fs. Several distinct jumps are visible in the figure, each having an approximate magnitude of 0.1 fs. The second 12-hour measurement showed similar results, although it did not contain as many sudden jumps. It is clear that the drift and jumps observed in the pointing stability measurements are of much lower magnitude than those seen in the delay stability measurements. Neither of the measurements contained any visible oscillations, especially not of 1-hour periodicity.
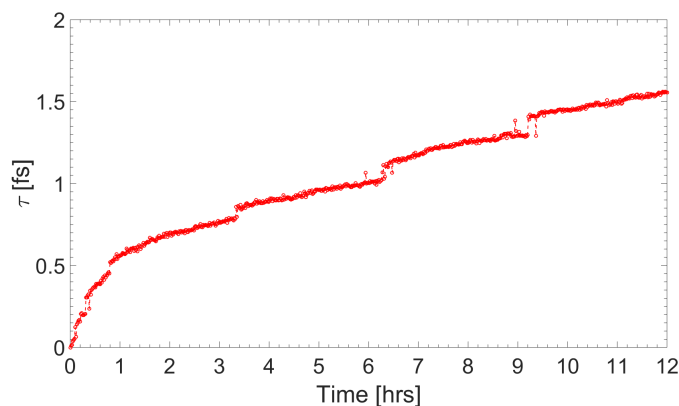

Figure 17: Pointing stability measurement conducted with the laser passing through the beam-expander, according to 6.3.1. Calculated change of delay as a function of time. Note the sudden jumps in the delay. After 12 hours an angular drift corresponding to almost 1.6 fs change of the delay has been accumulated. The sudden jumps have an approximate magnitude of 0.1 fs.

6.3.2 Without Beamexpander

The following results were obtained using the setup depicted in figure 9b. Again, two measurements spanning 12 hours were conducted, both with 60 s time resolution. A $f = 175\,\text{mm}$ and $f = 125\,\text{mm}$ lens respectively were used in the measurements. The results of these are presented in figures 18 and 19. The drift in figure 18 shows a similar behavior during the warm-up of the laser as found in complementing measurements of higher time resolution, with a maximum of 0.5 fs reached quickly, followed by a slower decay. This trend changes around the 4:th hour and after 12 hours a net delay drift of almost 0.5 fs has been accumulated again. The second measurement (see figure 19) showed a very different behavior: it lacked the characteristic warm-up sequence found in the other measurements and accumulated a much larger delay drift ($\sim 5.5\,\text{fs}$) over the course of 12 hours.

It is difficult to interpret the results of these measurements as they do not form any coherent picture. This situation is worsened by the results of a measurement conducted directly after the one presented in figure 19, with the only difference that the lens was removed, which showed no sign of drift at all. Nonetheless, these measurements still do

not feature any sudden jumps or 1-hour periodic oscillations, nor is the magnitude of any of the observed delay drifts comparable to that found in section 6.2.

The pointing stability measurements are not unequivocal, and more advanced tests are required to elucidate the different behaviors found. Even so, nothing was found indicating the laser beam wander as the cause of the observed delay features in section 6.2. Due to the limited time available, further investigations could not be performed. As a consequence the question as to the cause(s) of said features must be left unanswered at this point.

Figure 18: Pointing stability measurement conducted with the beam entering directly into the camera through a $f = 175\,\text{mm}$ lens, according to section 6.3.2. Calculated change of delay due to total angular drift as a function of time. Note the distinct warm-up behavior.
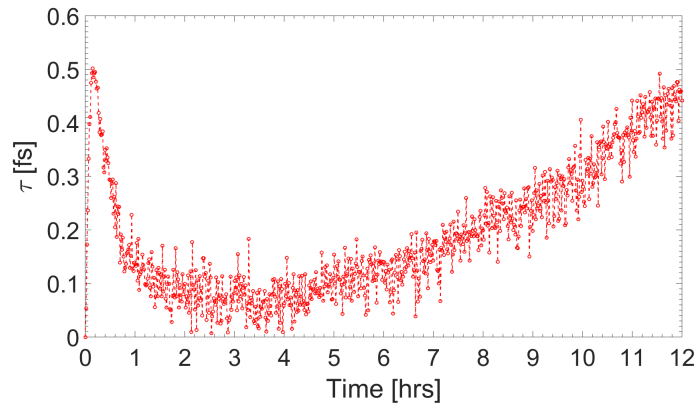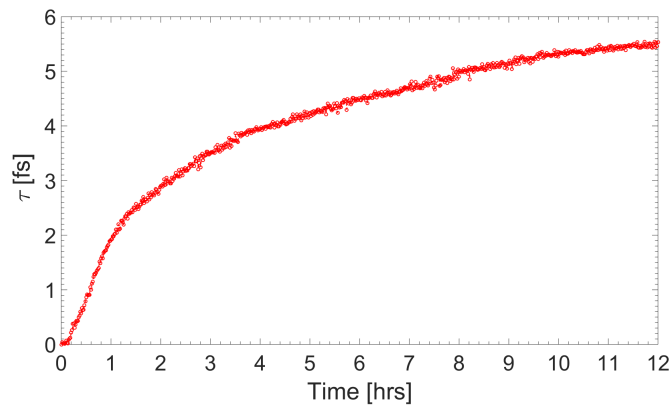

Figure 19: Pointing stability measurement conducted with the beam entering directly into the camera through a $f = 125\,\text{mm}$ lens, according to section 6.3.2. Calculated change of delay due to total angular drift as a function of time. Note the marked difference to figure 18.

7 Summary and Outlook

This final section will summarize the results of the thesis and give recommendations for future work related to the studied interferometer.

The results presented in this thesis provide conclusive evidence that the proposed and constructed interferometer design works, in the sense that an interference pattern of quality sufficient for long term delay determination was obtained (section 6.1). The main factor determining the quality of the interference pattern was found to be the hole-drilled recombination mirror; smoother holes will likely give a more symmetric and clear pattern. However, the quality of the mirror used evidently sufficed.

The stability of the interferometer was measured in terms of the delay derived from the formed interference pattern. The measured delay was found to exhibit four characteristic features: 1) rapid fluctuations with a standard deviation of $\sim 0.85\,\mathrm{fs}$, 2) sudden jumps of 2-4 fs, 3) oscillations with a period of ~ 1 hour and amplitude of $\sim 4\,\mathrm{fs}$, and 4) a linear drift of varying magnitude (section 6.2).

The rapid fluctuations are most likely caused by a combination of mechanical vibrations present in the laboratory and detector noise. The causes of the three other effects could not be definitively determined. Nevertheless, a few possibilities were excluded. Firstly, the sudden jumps have been shown to not be caused by inadvertent movements of the interferometer translation stage. Secondly, based on the seemingly smooth distribution of sudden jumps over time, it is deemed unlikely that their cause is direct human activity in or near the laboratory. To further seek the cause of these effects, the pointing stability of the HeNe laser used was investigated (section 6.3). Although both a net drift and the presence of sudden jumps of the beam position was found, their magnitude was too small to fully explain the effects observed in the delay stability measurements. Even so, a more stable co-propagating laser would at least not be detrimental to the stability of the interference pattern. No indications of oscillations of the required period were found in the beam wander. It is noteworthy that the measurements of the pointing stability, especially those described in section 6.3.2, form no consistent picture. Hence, the laser pointing stability could not be well-characterized and further investigations are called for before the angular drift can be decisively excluded as a cause of the anomalous effects observed in the delay stability measurements.

In order to more completely determine the possible effect of the beamexpander on the angular drift, an experiment in which two cameras and a beamsplitter are used to simultaneously monitor the beam passing through the expander and the one entering the camera directly could be devised. It would also be interesting to redo the delay stability measurements using a different laser unit to see if the same characteristic features can be observed. To the extent that it is possible, the setup should be tested in a more vibration-secure environment, to explore to what extent this influences the behavior of the measured delay and interference pattern stability. The angular drift simulations could be redone with the correct focal length of the probe arm focusing mirror used, to get a more accurate conversion factor of angular drift to delay shift.

The major next step in the development of this interferometer should, however, be to test it in actual RABITT-experiments, using an active delay stabilization. Only then will it be possible to truly evaluate the virtues of this interferometer setup.

8   Acknowledgments

I would first and foremost like to thank the division's coffee machine for many valuable late-night discussions. I would also like to extend my warmest thanks to my supervisor David Kroon for his support and willingness to discuss issues at all times of the day during this thesis. I am also very thankful to Anne L'Huillier for introducing me to the science of attosecond physics and giving me the opportunity to carry out this project.

Fredrik Bertilsson and Simon Ek deserve many thanks for fruitful discussions regarding theoretical questions in general and especially the deeper meanings of HHG.

References

[1] P. F. Moulton, J. G. Manni, and G. A. Rines. Spectroscopic and Laser Characteristics of Ti:Al$_2$O$_3$. *IEEE Journal of Quantum Electronics*, 3(1):125–132, 1986.

[2] D. Strickland and G. Mourou. Compression of amplified chirped optical pulses. *Optics Communications*, 56(3):219–221, 1985.

[3] A. Philippe, A. L'Huillier, and M. Lewenstein. Attosecond Pulse Trains Using High – Order Harmonics. *Physical review letters*, 77(7):1234–1237, 1996.

[4] P. M. Paul, E. S. Toma, P. Breger, G. Mullot, F. Auge, P. Balcou, H. G. Müller, and P. Agostini. Observation of a train of attosecond pulses from high harmonic generation. *Science (New York, N.Y.)*, 292(June):1689–1692, 2001.

[5] P. B. Corkum. Plasma Perspective on Strong-Field Multiphoton Ionization. *Physical review letters*, 71(13):1994–1997, 1993.

[6] Kathrin Klünder. *Electron Wave Packet Dynamics on the Attosecond Time Scale*. Media-Tryck, Lund, 2012.

[7] J. M. Dahlström, A. L'Huillier, and A. Maquet. Diagrammatic approach to attosecond delays in photoionization. *Physical Review B: Atomic, Molecular and Optical Physics*, 45, 2012.

[8] H. G. Müller. Reconstruction of attosecond harmonic beating by interference of two-photon transitions. *Applied Physics B: Lasers and Optics*, 74:S17–S21, 2002.

[9] K. Klünder, J. M. Dahlström, M. Gisselbrecht, T. Fordell, M. Swoboda, D. Guénot, P. Johnsson, J. Caillat, J. Mauritsson, a. Maquet, R. Taïeb, and a. L'Huillier. Probing single-photon ionization on the attosecond time scale. *Physical Review Letters*, 106(14):1–4, 2011.

[10] D. Guénot, D. Kroon, E. Balogh, E. W. Larsen, M. Kotur, M. Miranda, T. Fordell, P. Johnsson, J. Mauritsson, M. Gisselbrecht, K. Varjù, C. L. Arnold, T. Carette, A. S. Kheifets, E. Lindroth, A. L'Huillier, and J. M. Dahlström. Measurements of relative photoemission time delays in noble gas atoms. *Journal of Physics B: Atomic, Molecular and Optical Physics*, 47(24):245602, 2014.

[11] M. Chini, H. Mashiko, H. Wang, S. Chen, C. Yun, S. Scott, S. Gilbertson, and Z. Chang. Delay control in attosecond pump-probe experiments. *Optics express*, 17(24):21459–21464, 2009.

[12] Zerodur specifications. `http://www.schott.com/advanced_optics/english/products/optical-materials/zerodur-extremely-low-expansion-glass-ceramic/zerodur/index.html?so=scandinavia&lang=english`, 2014. [Online; accessed 11-05-2015].

[13] Specifications of the HeNe laser. `http://www.jdsu.com/en-us/Lasers/Products/A-Z-Product-List/Pages/laser-helium-neon-self-contained-1500-series.aspx`, 2015. [Online; accessed 13-05-2015].

A Recombination Mirror Drawing

Front   **Back**

Protected silver coating

Protected silver coating

⌀ 25.4

A A

⌀ 2.5   ⌀ 2.5

45°   45°   6

SECTION A-A

UNLESS OTHERWISE SPECIFIED: DIMENSIONS ARE IN MILLIMETERS SURFACE FINISH: TOLERANCES: LINEAR: ANGULAR:	FINISH:			DEBUR AND BREAK SHARP EDGES	DO NOT SCALE DRAWING		REVISION

	NAME	SIGNATURE	DATE			TITLE:		
DRAWN								
CHK'D								
APPV'D								
MFG								
Q.A				MATERIAL:		DWG NO.	Drilled mirror	A4
				WEIGHT:		SCALE:2:1	SHEET 1 OF 1	